Identifying the Colour of New Physics

A dissertation submitted to the University of Manchester for the degree of Master of Science by Research in the Faculty of Engineering and Physical Sciences

2011

Zhen Guo

School of Physics and Astronomy

Contents

Final word count: 10858

List of Figures

Abstract

In this study the effect of the different colour content of new colour-singlet and colour-octet TeV-scale resonances on radiation is examined using events with KK-photons and KK-gluons decaying to top pairs. It is found that the colour-singlet resonance produces more radiation than the colour-octet resonance, which is consistent with the theoretical study. The gap fraction and jet number are used to evaluate the amount of radiation. The jet number distribution in the interjet region shows that differences occur in the central region when energy flow between the two leading jets is above a threshold value. The effect of underlying event is studied by comparing results of events with and without underlying event. A study using the spherical harmonic power spectrum shows that there is a large difference between the power spectrum of final-state particles in the two (singlet/octet) cases. The difference between the power spectra of QCD jets and top jets is also examined.

Declaration

No portion of the work referred to in the dissertation has been submitted in support of an application for another degree or qualification of this or any other university or other institute of learning.

Zhen Guo
School of Physics and Astronomy
University of Manchester
Oxford Road
Manchester
M13 9PL
January 2011

Copyright

Acknowledgements

I would like to thank my supervisors, Jeff Forshaw and Thorsten Wengler, for their guidance, patience and encouragement. Special thanks to Jeff for his understanding and help. Thanks to Fred Loebinger for his great encouragement. I would also like to thank people in the ATLAS office for a lot of help. Also thanks to Stefan Ask for implanting KK-gluon and KK-photon into Pythia and answering to my questions about Pythia.

Thanks to Kiran Joshi for proofreading this dissertation.

Thanks to Pal Marius Bjornstad for a lot of discussions and suggestions.

Also thanks to all of the people in the group who have been so warm and nice. This is a really great opportunity to have been in this vibrant group and I will not forget.

Thanks to my family for their encouragement and support in all my life. Thanks to dad for many helpful discussions and to mum for her encouragement all the time.

Chapter 1

Introduction

As one of the significant puzzles of the standard model, the hierarchy problem invokes the building of new physics. The main solutions can be divided into two types: supersymmetry [1] and models with extra dimensions [2, 3]. In extra dimensional models, Kaluza-Klein(KK) excitations at the TeV scale are involved. Due to their heavy masses, the KK particles will immediately decay into standard model particles, which makes it hard to observe them directly. The probe of the KK particles is through their decay products. Top quarks are considered to be strongly coupled to the KK particles because of their large masses. The production channel $pp \rightarrow X \rightarrow t\bar{t}$ is thus dominant, and important for the LHC search of KK particles.

When the KK particle process is successfully extracted from the background events, an important issue is how to identify the colour of these new resonances. They are usually colour singlets or colour octets, which cause different soft gluon radiation patterns. This is the focus of this study. Among the gauge bosons, the KK-gluon(g^*) and the KK-photon(γ^*) are chosen for comparison, as they are both spin-1 particles and g^* is colour octet, while γ^* is colour singlet. In this study, the particles focussed on are g^* and γ^* at a mass of 2TeV in the Randall-Sundrum model [3], which is an extra dimensional model. Phenomenologically, the parameters of the two kinds of particles are chosen so that they have the same decay width and production cross section. The analysis is carried out using rapidity gap events defined by energy flow and the spherical harmonic power spectrum, which is inspired from its application in the CMB anisotropy [4].

This dissertation is organized as follows. Chapter two presents the en-

ergy flow analysis of the different radiation patterns of the g^* and γ^* events. In chapter three, the generic event structure is analysed using the spherical harmonic power spectrum. Finally, chapter four is the conclusion.

1.1 Pythia

Pythia 8 [5] is a general-purpose self-contained generator to generate high-energy collisions. It can simulate hard processes as well as initial- and final-state parton showers, multiple parton interactions, beam remnants, string fragmentation, particle decays and so on. It includes reactions within and beyond the standard model.

Initial- and final-state radiation showering is based on a p_T-ordered algorithm. Multiple parton interactions are included in the same p_T sequence. Hadronization is based on the Lund string fragmentation framework. The nature of the event is decided by the hard process, which is calculated in perturbation theory. At parton level, initial- and final-state radiation and multiple parton interactions are mainly controlled by perturbative physics but also involve some non-perturbative physics.

Non-standard physics has been implemented in Pythia since Pythia 6.4. The implementation of KK-gluons(g^*) is in accord with the RS1 scenario [6]. Currently, there is one process for g^*, where it is produced by $q\bar{q}$ fusion. The γ^* resonance is modelled analogously to the Z' process, and it only couples to light and top quarks. The couplings are set so that it is equivalent to a heavy photon. The couplings are also tuned to give a similar cross section and width to those of the g^*. The cross section before any cuts is 785.9 fb for g^* events and 1101 fb for γ^* events. The widths are around 400GeV.

1.2 New Heavy Resonances

The RS model is an attractive model which proposes one warped extra dimension to solve the hierarchy problem naturally [3]. There are two 3-branes embedded in five dimensions, TeV brane and Planck brane. Gravity and standard model fields can propagate in the bulk. The bulk in between the two branes is the extra fifth dimension. The solution is derived from the five-dimensional Einstein's equations, with the metric satisfying four-dimensional

Poincaré invariance, which takes the form

$$ds^2 = e^{-2k|y|}\eta_{\mu\nu}dx^\mu dx^\nu - dy^2 \tag{1.1}$$

in which $y = r_c\phi$ is the coordinate of the 5th dimension. The brane at $y = 0$ is the Planck brane and the one at $y = \pi r_c$ is the TeV brane. r_c is the compactification radius which sets the size of the extra dimension. k is a scale of order Planck scale.

A phenomenological prediction of the RS1 scenario is the existence of heavy KK mode particles of TeV scale. Since KK gauge bosons are singly produced, they have a larger production rate than KK quarks [7]. As for the KK particles studied in this dissertation (g^* and γ^*), the dominant production channel is through the annihilation of $u\bar{u}$ and $d\bar{d}$ from the protons. Since the light fermions are localized near the Planck brane, their couplings to KK particles are very small compared to the couplings in the standard model [8]. This leads to a small production cross section compared to QCD processes. Several studies have been undertaken to separate the signal from the QCD background [6, 7, 9], which is outside the scope of this dissertation. Among the KK gauge bosons, g^* has the strongest coupling to proton constituents. It is likely to be discovered first with the largest production rate [3]. There is also a possible production channel via gluon-gluon fusion induced by heavy quark loops. It exists in higher order of perturbation theory so the production cross section is smaller. Due to orthogonality, the coupling is zero at tree level. This production channel is not included in this analysis. Since the top quark is heavy and localized near the TeV brane, the couplings of the KK mode resonances to $t\bar{t}$ are largely enhanced compared to other SM particles. As a result, the KK mode resonances decay exclusively to $t\bar{t}$.

The KK-photon(γ^*) is the KK partner of the hypercharge gauge boson [10]. It is a spin-1 colour-singlet gauge boson, in contrast to the colour-octet nature of g^*. This property motivates our study of the different radiation patterns between colour singlets and colour octets.

1.3 Energy and Colour Flow

In QCD, partons interact via the exchange of colour. The colour charge should be conserved in each process. Based on this point, the different patterns of the exchange, or flow of colour, can be used to study processes mediated by exchange of a colour-singlet or colour-octet, which decays into a high p_T pair of boosted top jets.

This field of study takes place in an invariant phase space with variables rapidity y(or pseudorapidity η), azimuth angle ϕ and transverse momentum p_T(or transverse energy E_T). In experiment, η is usually used instead of y as a massless limit approximation, and it is related to the polar angle, θ, via $\eta \equiv -\ln[\tan(\theta/2)]$.

Colour flow between the two jets produced by colour-singlet or colour-octet particles will have an effect on both the jet substructure and radiation between them. Studies of radiation between jets focus on dijet gap events which contain a rapidity gap [11, 12, 13, 14, 15, 16]. A rapidity gap is defined as a region between the two leading jets which has limited hadronic activity. Another requirement of dijet gap events is that the rapidity difference of the two leading jets is sufficiently large. The reason for this requirement is that the boundaries of the rapidity gap region are defined at the inside edges of the two leading jets; a large gap ensures that the phase space is large enough.

Dijet events with a large rapidity gap are of particular interest to new physics research. It was first suggested to study the Higgs Boson in such events by Dokshitzer, Khoze and Troyan [17]. Then Bjorken [18] explored its further application in electroweak boson exchange and the survival of the rapidity gap. He also discussed jets and rapidity gaps in strong-interaction processes. The result shows that radiation in the central region between the two high E_T jets is highly suppressed in the case of colour-singlet exchange in the t-channel. Since then, rapidity gap events have been considered as a useful tool to investigate colour-singlet exchange processes. It is noted that Higgs production via the WW channel can be identified by analysing the radiation pattern of events with a rapidity gap [19]. Rapidity gap events are found at the Tevatron and HERA in about 10% of the total events [20, 21].

In early research, multiplicity was used to identify rapidity gaps [22]. Multiplicity could be the number of cells in the calorimeter which receive transverse

energy larger than a set value. A rapidity gap event is an event with zero or low multiplicity in the interjet region between the two leading jets. In recent years, Oderda and Sterman proposed the use of energy flow Q_c in the interjet region to define rapidity gap events [13]. Q_c is the energy away from the hard jets mediated by soft gluon radiation. This choice could partly avoid the problems of soft radiation from spectator hard interactions and the colour of hard scattering affected by soft gluon radiation. Q_c is an infrared safe variable. The factorized cross section $d\sigma/dQ_c$ as a function of Q_c is calculated for t-channel colour-singlet and colour-octet processes. The result shows that in a mixed cross section, the singlet component mainly contributes to small energy flow while the octet one dominates at large energy flow.

Recently, Ilmo Sung extends the application to s-channel processes through heavy new resonance exchange [23]. The techniques of factorization and resummation are used to derive the partonic cross section in terms of the mass of the exchange particle M, the rapidity difference between the two leading jets $\Delta\eta$, the strong coupling α_s and the energy flow threshold in the interjet region Q_0. The calculation includes all possible partonic processes. The quantity studied is the gap fraction, defined as the ratio of the number of events with energy flow in the interjet gap region up to a given value to the number of total events. However, Sung's calculation is only at parton level and does not even include the incoming hadrons.

In Sung's study, the gap fraction has been studied for spin-1, spin-0 and 2 resonances. In the spin-1 part, the gap fractions f_{gap} of colour-singlet Z' and colour-octet G' events are compared at different invariant mass and dijet rapidity difference. The decay to a top pair or a bottom pair is considered, and this is shown in figure 1.1. Here Q_0 starts from zero, though $Q_0 < 10\text{GeV}$ is hard to detect at the LHC. From the results, $f_{gap}^{G'}$ is always higher than $f_{gap}^{Z'}$, which is contrary to the results from t-channel processes studied before, but not unexpected. At low Q_0, $f_{gap}^{G'}$ increases rapidly compared to $f_{gap}^{Z'}$, and fewer colour-singlet events accumulate at low Q_0. The gap fractions of events where products are bottom quarks are slightly smaller compared to those of top quarks with other parameters the same. This difference becomes larger when the resonance mass is smaller. The ratio of the gap fractions, $f_{gap}^{G'}/f_{gap}^{Z'}$, depends on the rapidity range of the gap region rather than $\Delta\eta$. These phenomena can be understood by naive colour flow arguments as we now discuss.

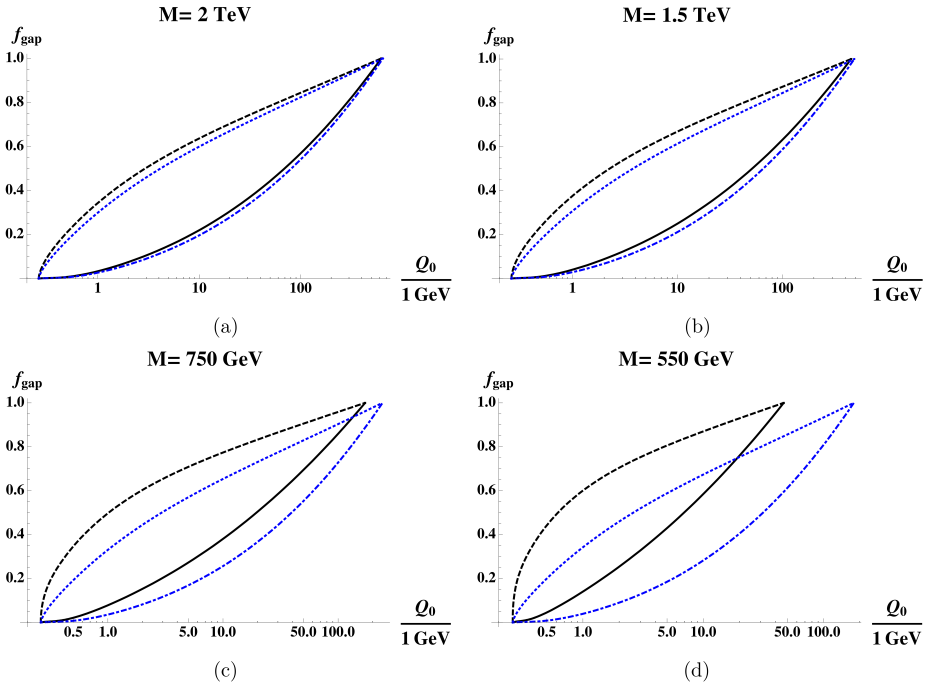

Figure 1.1: [figure from [23]]Gap fractions identified by energy threshold Q_0 at $\Delta\eta = 2$ and interjet region $Y = 1.5$ for resonance masses $M = 2, 1.5, 0.75, 0.55$TeV. The solid curves describe gap fractions of Z' events, the dashed curves for G' events that decay into a top pair. The dot-dashed curves(blue) describe the gap fraction of Z' events, and the dotted curves(blue) for G' events that decay into a bottom pair.

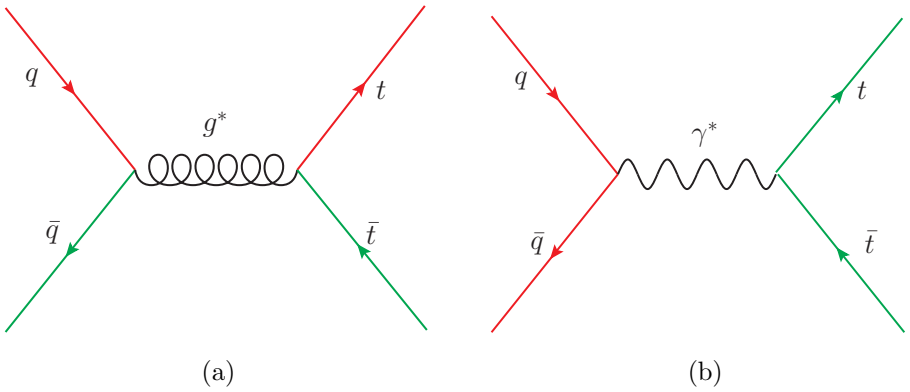

Figure 1.2: The Feynman diagrams show the s-channel processes in which a quark pair annihilates into a KK-particle. The coloured lines denote the colour flow between the incoming proton constituents and outgoing top quarks. (a)$q\bar{q} \to g^* \to t\bar{t}$ and (b)$q\bar{q} \to \gamma^* \to t\bar{t}$.

The pattern of soft gluon radiation can be explained using colour flow. Figure 1.2(a) shows the configuration of colour flow for the process $pp \to g^* \to t\bar{t}$. Each proton contributes one parton with a different colour. The partons annihilate to produce the g^*. The top pair products have colour which is consistent with the g^*. At the leading order, they are each colour connected with one initial parton. As the incoming parton's momentum is in the beam direction, in rapidity space, the "bremsstrahlung" gluons are radiated into the region between the top pair products and the beam direction, such that an interjet rapidity gap is formed.

The colour structure of colour-singlet exchange is shown in figure 1.2(b). Two same-colour partons, each from one proton, annihilate into the γ^*. The top quarks form a colour singlet, which leads to a colour string between them. As a result, the resulting bremsstrahlung will mainly fill the rapidity region between the dijets, such that no gap is formed. In addition, the two incoming quarks also constitute a colour singlet. Soft gluons are possibly radiated into the region between the top jets and the beams.

1.4 QCD Radiation

Soft wide-angle radiation is a kind of QCD radiation. In QCD radiation, quarks or gluons radiate a gluon with a colour charge, leaving the colour of the original parton changed. Because of QCD confinement, gluons and quarks cannot exist freely. A free parton will generate a parton shower by radiation and with quark pairs created from the vacuum. This collinear formation will finally turn out to be jets, which we observe in the detector and use to study the mechanism of QCD radiation.

In the calculation of the cross section of gap events, the energy flow threshold in the interjet region is chosen to be $E_T^{cut} \gg \Lambda_{QCD}$, in which Λ_{QCD} is the scale boundary of non-perturbative and perturbative QCD. Then the cross section can be calculated using perturbative QCD. Including the energy scale of the hard jets, there are three scales in total, $E_{jets} \gg E_T^{cut} \gg \Lambda_{QCD}$.

In simulations of QCD radiation, currently the method of matching parton showers and matrix elements is used. Parton showers are good at describing collinear and soft radiation. Parton showers can be wrong by orders of magnitude for hard radiation. Matrix elements are mainly used for high energy

far-split radiation at short distance. For a good match, the soft region and hard region should be well separated and double counting by the equivalent phase space configuration should be avoided.

1.4.1 Underlying Event

The underlying event(UE) contains everything except components from the hard process. The interesting processes in an event are usually the hard process, its hadronization, decay plus initial-state radiation(ISR) and final-state radiation(FSR). The UE is approximately a combination of multiple parton interactions(MPI) and soft beam remnants interactions. In this study, UE refers to MPI as simulated in Pythia.

The UE is a problem in the study of hard processes. It is unavoidable in a real event. Since non-perturbative QCD is involved, the UE is the least known part of the interaction and is not as accurately modelled as other processes in Monte Carlo simulations. It could contaminate the signal in searches for new physics. In MPI, parton pairs which are not in the hard process can undergo scattering. Most of the scatterings are, however, soft scatterings involving non-perturbative QCD. The beam remnants are parts of the hadron which are not involved in ISR or hard scattering and left behind. Due to the colour connection, the beam remnants could change the colour structure of the hard process [24]. They may make the unrelated colours and anti-colours taken from the beam connect to each other and thus change them.

In the analysis, the results of events with and without UE are compared to determine the effect of UE.

1.5 Power Spectrum

A spherical harmonic expansion is the decomposition of a distribution $f(\theta, \phi)$ on the sphere into harmonics of different scales.

$$f(\theta, \phi) = \sum_{l} \sum_{m=-l}^{m=l} a_{lm} Y_{lm}(\theta, \phi) \tag{1.2}$$

where $Y_{lm}(\theta, \phi)$ are the spherical harmonics, see section 3.1 for the definitions of $Y_{lm}(\theta, \phi)$ and more discussion. The level of accuracy which the transformation

achieves can be obtained by truncating the expansion to a certain degree l. The coefficient a_{lm} has two indices l and m. l corresponds to the wavelength of the harmonic on the sphere, and m is related to the orientation of the polar angle. The power spectrum is defined as

$$C_l = \frac{1}{2l+1} \sum_{m=-l}^{m=l} a_{lm}^* a_{lm} \tag{1.3}$$

It depends only on l.

The power spectrum is used in many areas to research anisotropy, such as in geophysics and cosmology. In geomagnetics, power spectra are used for numeric geomagnetic field analysis [25, 26]. Core and crustal fields have different dimensions, corresponding to different polynomials in the harmonic expansion. In cosmology, spherical harmonics are used to describe the anisotropy on the celestial sphere. The power spectrum contains the same information as a two-point correlation function $\langle f(\theta_1, \phi_1), f(\theta_2, \phi_2) \rangle$. It could describe temperature, hadron density or other quantities. The temperature fluctuation, $\delta T/T$, in the cosmic microwave background is theoretically predicted and experimentally found to follow a Gaussian distribution [27, 28, 29]. When the temperature fluctuation is expanded in spherical harmonics, the coefficients also obey a Gaussian distribution. The correlation function of CMB anisotropy is defined as

$$C(\theta_{12}) = \left\langle \frac{\delta T(\boldsymbol{e}_1)}{T} \frac{\delta T(\boldsymbol{e}_2)}{T} \right\rangle \tag{1.4}$$

where θ_{12} is the angle between the directions $\boldsymbol{e}_1$ and $\boldsymbol{e}_2$. The correlation function can be derived as

$$C(\theta) = \sum_l \frac{2l+1}{4\pi} C_l P_l(\cos\theta) \tag{1.5}$$

where the multipole coefficients C_l define the CMB power spectrum. P_l are associated Legendre polynomials, see section 3.1 for more discussion. Parameters in the theoretical model could be determined from the fit of the power spectra from experiment and theory.

The power spectrum has been used to discriminate signals of new physics. To discriminate the signal of highly excited squirk bound states, which generating photon radiation, from minimum bias events, the power spectra of

energies deposited on a toy calorimeter are compared [30]. The multipole of degree $l = 2$ dominates in the new physics signal and multipoles are evenly distributed for the minimum bias one, as shown in figure 1.3. A variable describing the level at which multipoles of low degree differ from the other low-degree multipoles is proposed. The difference between new physics events and minimum bias events is significant.

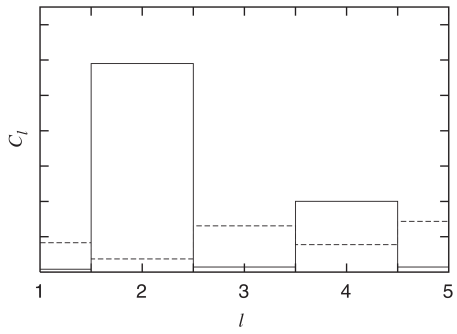

Figure 1.3: [figure from [30]]Multipole expansion of energy distribution in a toy calorimeter in production and decay of the squirk excited bound states(the solid line) and the minimum bias event(the dashed line).

Fourier transformations have also been used to resolve correlations in particle physics events on different physical scales [31]. The imaginary coefficients are found to peak at different degrees between QCD di-jet and colour-singlet exchange events.

Energy correlations in event evolution are closely connected with QCD dynamics. Many researchers are trying to distinguish events or extract parameters in QCD dynamics based on energy correlations. Most of them are working in perturbative QCD. Event shape variables are sensitive to characteristics of QCD radiation. They play a crucial role in understanding the dynamics of hadronization [32]. In a study aimed at discriminating highly boosted top jets from QCD background, template methods based on correlations of energy flow have been used [33]. In conformal field theory, long distance energy correlations in collisions have been studied using the stress tensor [34].

The energy correlation in g^* and γ^* events is different, stemming from the different radiation pattern caused by the colour difference. To investigate the energy correlations, the power spectrum, which is equivalent to a two-point

correlation function, is a new and interesting tool to explore. We shall return to this in Chapter 3.

Chapter 2

Using Jets and Energy Flow

In this chapter, $pp \to g^*/\gamma^* \to t\bar{t}$ processes are studied by looking at additional jets and energy flow. The top quarks can decay either hadronically or leptonically. Rapidity gap events are the focus of investigation. The rapidity gap is defined in two ways: 1.there is no jet with p_T above a given value in the interjet region, which is between the inside edges of the top jets; 2.the energy flow, which is the sum of transverse energies of all final-state particles in the interjet region, is less than a certain value. As rapidity gap events require large rapidity difference between the two leading jets, events with a pseudorapidity difference between the two leading jets, denoted as $\Delta\eta$, larger than 2 are selected. The fraction of events decreases dramatically with increasing $\Delta\eta$. For the data sample used, the proportion of events with $\Delta\eta > 3.0$ is 0.095 for g^* events and 0.073 for γ^* events. When $\Delta\eta > 4.0$, it is 0.0216 for g^* events and 0.0135 for γ^* events. The cross section before any cuts is 785.9 fb for g^* events and 1101 fb for γ^* events. Assuming that the LHC has 10 fb^{-1} of data, there would be 58 and 47 events with $\Delta\eta > 3.0$, 13 and 9 events with $\Delta\eta > 4.0$ of g^* and γ^* events respectively. We need enough events to study the cases with large $\Delta\eta$. In this study, comparisons are made between results from events with and without UE to find the uncertainties due to the UE.

2.1 Monte Carlo Generation

Pure $pp \to g^*/\gamma^* \to t\bar{t}$ events are generated in Pythia 8, both with and without UE. The resonances have masses of 2TeV and width around 400GeV. Events with KK-particles in a narrow mass window $1980 - 2020$GeV are selected at

the generation level to make the event samples as similar as possible. The cross section for g^* to have mass at $1980 - 2020$GeV is 60.9 fb and 59.0 fb for γ^*. The couplings of KK-particles to quarks were tuned to make the cross section and width of g^* and γ^* similar.

2.2 Definition

The analysis is done in rapidity space. The top jets are found by fastjet [35] using the anti-kt algorithm [36] with radius $R = 0.7$ and identified as the two jets with largest p_T. The pseudorapidities of the two top jets are η_{jet1} and η_{jet2}. Their pseudorapidity difference is the absolute difference $\Delta\eta = |\eta_{jet1} - \eta_{jet2}|$. The interjet region is the region between the inside edges of the top jets, which is shown in figure 2.1. The width of the interjet region is $\Delta\eta - 0.7 \times 2$. The rapidity range Δy is centred at the middle of the interjet region. The jet region is two rapidity belts in the range of $(\eta_{jet1} - 0.7, \eta_{jet1} + 0.7)$ and $(\eta_{jet2} - 0.7, \eta_{jet2} + 0.7)$. The away region is outside the outer edges of the top jets. The width of this region is 2 in pseudorapidity on each side. The study is in a frame in which $\eta_{jet1} = -\eta_{jet2}$. As shown in figure 2.1, the coordinate for illustration of the distribution in the interjet region is η_1, with the origin at the midpoint of η_{jet1} and η_{jet2}, denoted by $\eta_{mid} = (\eta_{jet1} + \eta_{jet2})/2$. η_1 corresponds to η, the pseudorapidity in the lab frame, with $\eta_1 = \eta - \eta_{mid}$. The coordinate for illustration in the away region is η_2, with the origin at the outer edges of the top jets in the two away regions. The coordinate η_2 is positive in both away regions. The values on each side, which are at the same distance from the corresponding origin, are overlaid.

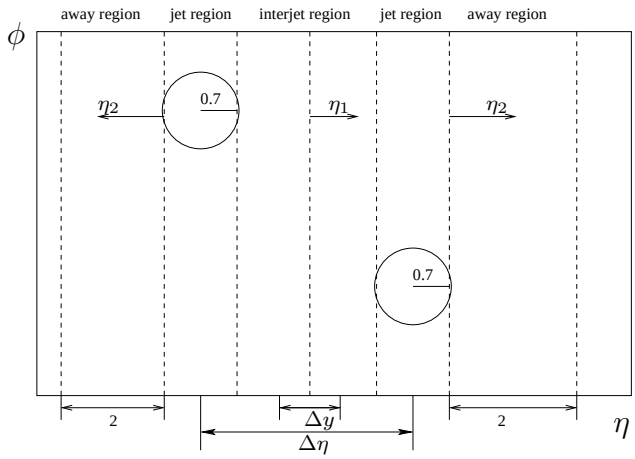

Figure 2.1: The regions defined in the analysis.

2.3 Analysis Using the Jets

In this part, all final-state particles are clustered into jets. Particles not in the top jets are clustered using the anti-kt algorithm with radius $R = 0.4$. g^* and γ^* events with $\Delta\eta$ at $2.0, 2.5, 3.0, 3.5, 4.0$(with a spread of 0.1, e.g. 1.9 to 2.1) are selected and compared.

2.3.1 Gap Fractions

The gap fraction is defined as the ratio of the gap events to the total events. Here the gap events are events with an interjet region absent of jets with p_T larger than a given value.

When studying events with UE, the threshold of the jet p_T in the gap definition, denoted by p_T^{cut}, is selected to be several values: $10, 20, 30$GeV. Though jets with $p_T < 20$GeV are hard to measure by the LHC detectors, they are studied theoretically. The gap fraction is a function of the rapidity range Δy at a certain $\Delta\eta$ and p_T^{cut}. As expected, colour-octet g^* events always have a higher gap fraction than colour-singlet γ^* events, which is illustrated in figure 2.2. The gap fraction at rapidity range $\Delta y = \Delta\eta$ will decrease when $\Delta\eta$ increases. While at the same Δy, f_{gap} is higher when the interjet region $\Delta\eta$ increases, which means that there are more jets with $p_T > p_T^{cut}$ per phase-space unit when $\Delta\eta$ is smaller.

Gap fractions corresponding to different p_T^{cut} are compared between g^* and

γ^* events in figure 2.3. The gap fraction curve will turn from concave to convex, at fixed $\Delta\eta$ and increasing p_T^{cut}, or fixed p_T^{cut} and increasing $\Delta\eta$. The increase in the absolute value of the slope of the gap fraction curve indicates that the probability of jets with $p_T > p_T^{cut}$ being distributed in the rapidity range where the slope increases is higher. According to this, large p_T jets tend to be distributed close to the inside edges of the top jets in both g^* and γ^* events. Our observations imply that the distribution of jets with $p_T > p_T^{cut}$ is different for the two and jets in γ^* events generally have larger p_T than those in g^* events.

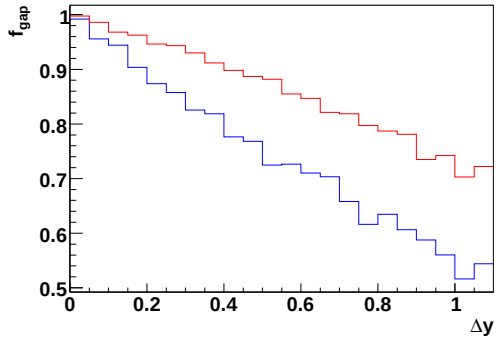

(a)

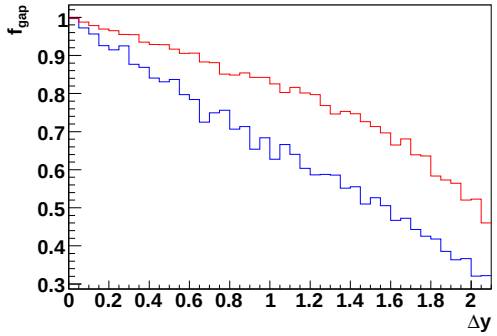

(b)

Figure 2.2: Gap fractions of events with UE turned on as functions of rapidity range defined by absence of jets with $p_T > p_T^{cut}$. (a)$\Delta\eta = 2.5$, $p_T^{cut} = 30$GeV and (b)$\Delta\eta = 3.5$, $p_T^{cut} = 30$GeV. Red lines are for g^* events and blue lines are for γ^* events.

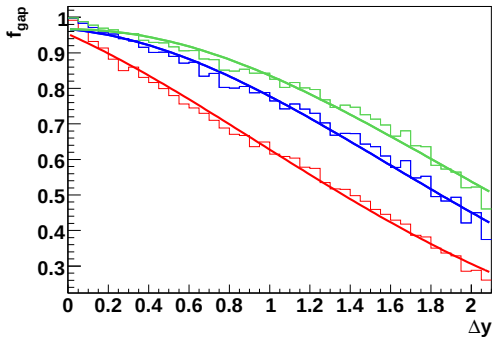

(a)

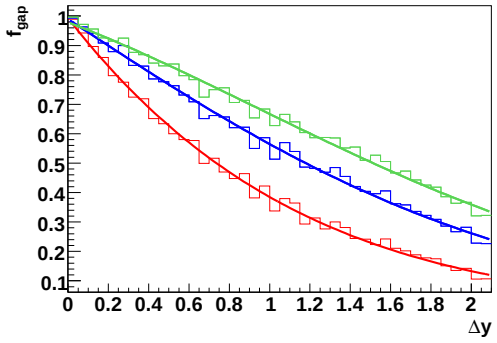

(b)

Figure 2.3: Comparisons of gap fractions with UE turned on at different p_T^{cut}, $\Delta\eta = 3.5$. Gap fractions of (a)g^* events and (b)γ^* events, from lower to higher, $p_T^{cut} = 10, 20, 30$GeV.

The UE reduces gap fractions in both g^* and γ^* events. The effect of the UE on gap fractions as a function of Δy is more apparent when $\Delta\eta$ is small, as shown in figure 2.4. However, the effect of the UE is not enough to spoil the difference. Gap fractions as a function of p_T^{cut} show that the UE could spoil the discriminating ability at low p_T^{cut} when $\Delta\eta$ is small.

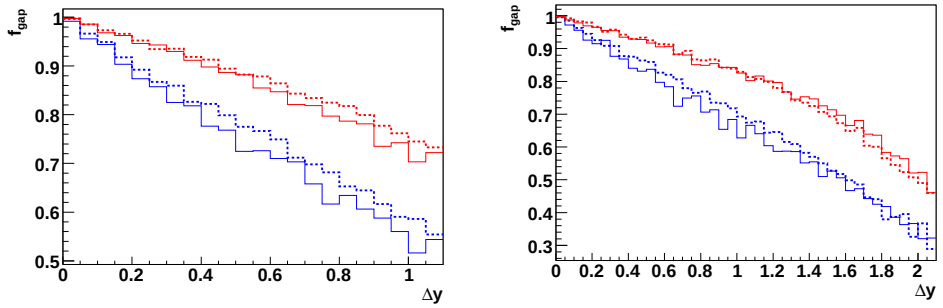

(a) (b)

Figure 2.4: Comparisons between the gap fractions of events with and without UE as a function of Δy with $p_T^{cut} = 30\text{GeV}$, at (a)$\Delta\eta = 2.5$ and (b)$\Delta\eta = 3.5$. The red solid lines are for $f_{gap}^{g^*}$ with UE. The red dashed lines are for $f_{gap}^{g^*}$ without UE. The blue solid lines are for $f_{gap}^{\gamma^*}$ with UE. The blue dashed lines are for $f_{gap}^{\gamma^*}$ without UE.

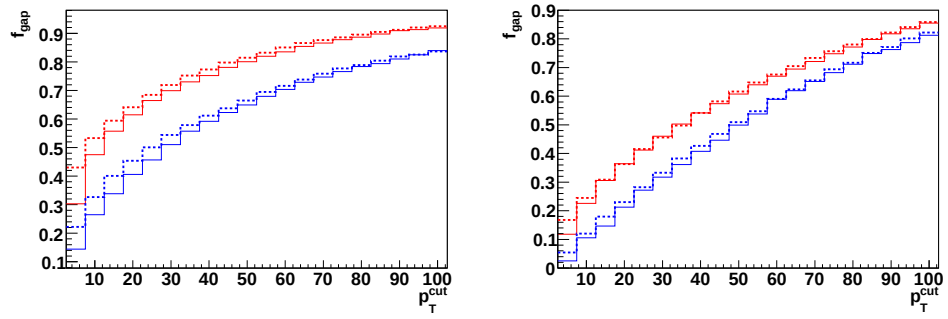

(a) (b)

Figure 2.5: Comparisons between gap fractions of events with and without UE as a function of p_T^{cut}, at (a)$\Delta\eta = 2.5$ and (b)$\Delta\eta = 3.5$. The red solid lines are for $f_{gap}^{g^*}$ with UE. The red dashed lines are for $f_{gap}^{g^*}$ without UE. The blue solid lines are for $f_{gap}^{\gamma^*}$ with UE. The blue dashed lines are for $f_{gap}^{\gamma^*}$ without UE.

2.3.2 Jet Number

Jet number is important as it is a direct manifestation of the dynamics of QCD [37]. Because of the colour connection between the initial quark pair and final top pair, generally, γ^* events have more radiation in the whole space, which corresponds to a larger jet number.

The differences in jet number with $p_T > p_T^{cut}$, denoted by N_{jet}, mainly exist in the interjet region and the jet region, which is the pseudorapidity region which contains the two leading jets. In the interjet region, γ^* events aways have a larger N_{jet}. When $\Delta\eta$ increases, the proportion of events which contain jets with $p_T > p_T^{cut}$ increases for both kinds of events, as shown in figure 2.6. The UE increases N_{jet} in the interjet region. At $\Delta\eta = 3.5$, the proportion of γ^* events with $N_{jet} = 1$ is slightly smaller than that of g^* events, while it is larger for events with UE. This indicates that the uncertainty of the UE may spoil the discriminating ability of the gap fraction if there is one jet with $p_T > p_T^{cut}$ in both g^* and γ^* events at large $\Delta\eta$.

As for the jet region, the proportion of events with a jet region which contains jets $p_T > 30$GeV is compared. The difference is apparent when $\Delta\eta$ is small, as shown in figure 2.7. When $\Delta\eta = 2, 2.5$, the proportions of γ^* events are much larger. However, the difference between the proportions is small when $\Delta\eta \geq 3$. In the away region, the difference between N_{jet} of g^* and γ^* events is small, as shown in figure 2.8.

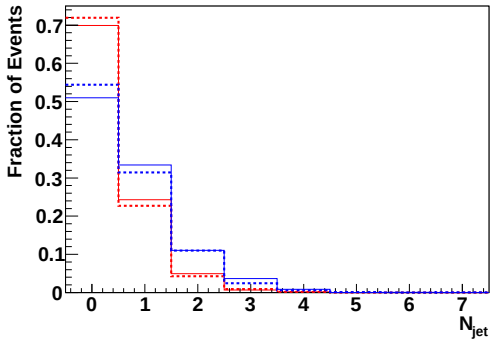

(a)

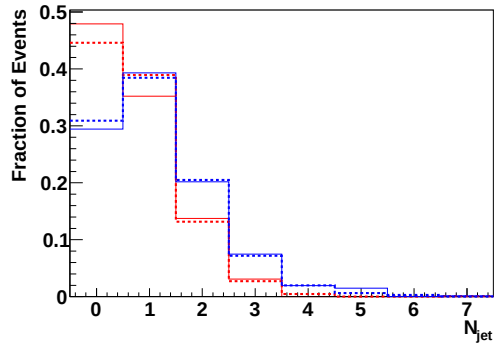

(b)

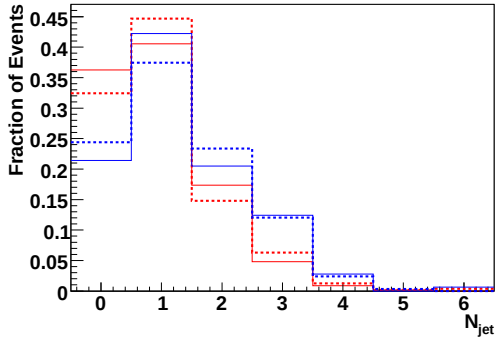

(c)

Figure 2.6: Comparisons of the jet number with $p_T > 30$GeV in the interjet region in events with and without UE. (a)The jet number at $\Delta\eta = 2.5$. (b)The jet number at $\Delta\eta = 3.5$. (c)The jet number at $\Delta\eta = 4.0$. Red solid lines are for g^* events with UE. Red dashed lines are for g^* events without UE. Blue solid lines are for γ^* events with UE. Blue dashed lines are for γ^* events without UE.

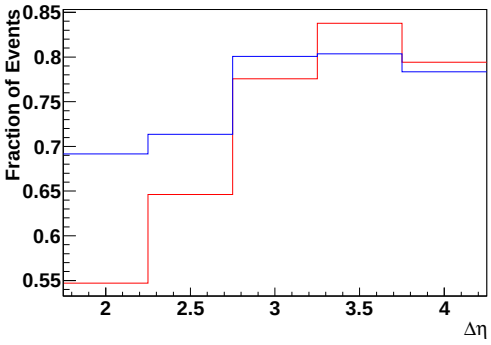

Figure 2.7: Proportion of events with UE in which the jet region contains jets with $p_T > 30$GeV. The red line is for g^* events. The blue line is for γ^* events.

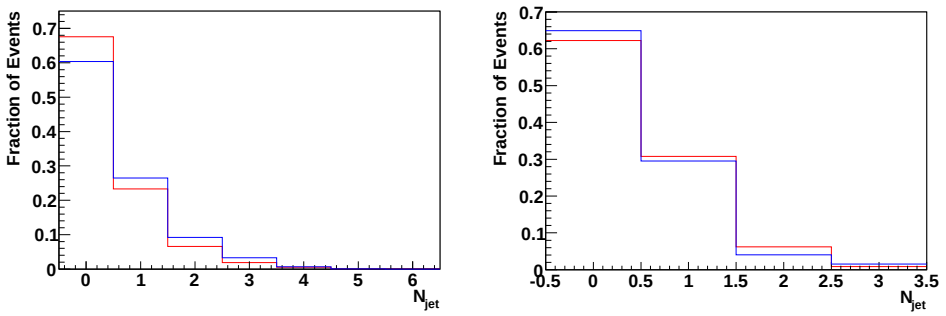

(a) (b)

Figure 2.8: N_{jet} with $p_T > 30$GeV in the away region in events with UE at (a)$\Delta\eta = 2.5$ and (b)$\Delta\eta = 4.0$. The red lines are for g^* events. The blue lines are for γ^* events.

2.3.3 Distribution of the Jet Number

Another consequence of the different colour flow in g^* and γ^* events could be the probabilities of the positions at which additional jets appear in the interjet region. The difference of the shape of the gap fraction curve shown in the section on gap fractions have indicated that the distributions are different. In this section, the distribution of N_{jet} is examined.

The average number of jets with $p_T > p_T^{cut}$, denoted by $\bar{N}_{jet}$, in events containing such jets in the interjet region, is compared here. Generally, $\bar{N}_{jet}$ for g^* events is less than that of γ^* events. As shown in figure 2.9, in the interjet

region, the probabilities of jets to appear close to the top jets are similar in g^* and γ^* events. There is a difference in the central interjet region, where γ^* events have larger probability to contain the jets. This result indicates the difference between the jet distribution of g^* and γ^* events in which there are jets with $p_T > p_T^{cut}$ in the interjet region.

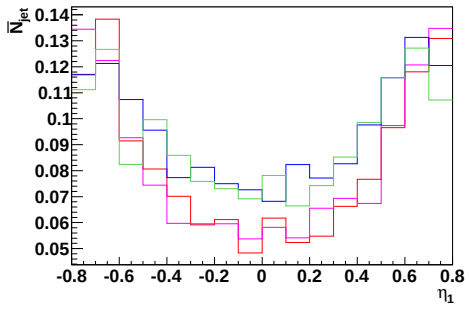

Figure 2.9: Distribution of $\bar{N}_{jet}$ with $p_T > 30$GeV in the interjet region at $\Delta\eta = 3.0$, in events with and without UE. The red line is for g^* events with UE. The pink line is for g^* events without UE. The blue line is for γ^* events with UE. The green line is for γ^* events without UE. The origin of coordinate η_1 is at the midpoint of η_{jet1} and η_{jet2}.

In the away region, the distributions of $\bar{N}_{jet}$ with $p_T > 30$GeV are similar for g^* and γ^* events, as shown in figure 2.10. The distribution of $\bar{N}_{jet}$ with $p_T > 10$GeV falls down rapidly as η_2 increases. The distribution of g^* events is not significantly higher than the γ^* one, as the colour flow arguments argue that the top products are colour-connected to the beams. This may come from two effects. One effect is that though at leading order the top products are colour-connected to the beam, in reality initial-state radiation reduces the colour-connection effect. The other is that the colour connection between the jets and the beams may cross. Beside, the light fermion pair which produces the γ^* is colour-connected, which increases the radiation over all phase space.

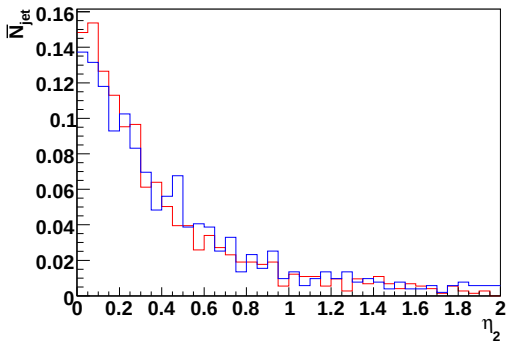

Figure 2.10: Distribution of the number of jets with $p_T > 30$GeV at $\Delta\eta = 3.0$ in the away region in events with UE. The red line is for g^* events. The blue line is for γ^* events. The origin of the coordinate η_2 is at the outer edges of the top jets.

2.3.4 p_T Distribution

In this section, the average p_T distribution of all jets is shown. The jet p_T is filled at the centre of the jet. The p_T distribution averaged over all events is the average p_T distribution, denoted by $\bar{p}_T$. In the interjet region, the difference between the p_T distribution of g^* and γ^* events is large in the whole region when $\Delta\eta$ is small. As $\Delta\eta$ increases, the difference in the region close to the top jets decreases. The difference is mainly in the central region when $\Delta\eta$ is large, as illustrated in figure 2.11(a)(b). In the away region, the p_T distribution of g^* events will increase when $\Delta\eta$ increases, shown in figure 2.11(c)(d). This is consistent with the colour flow arguments.

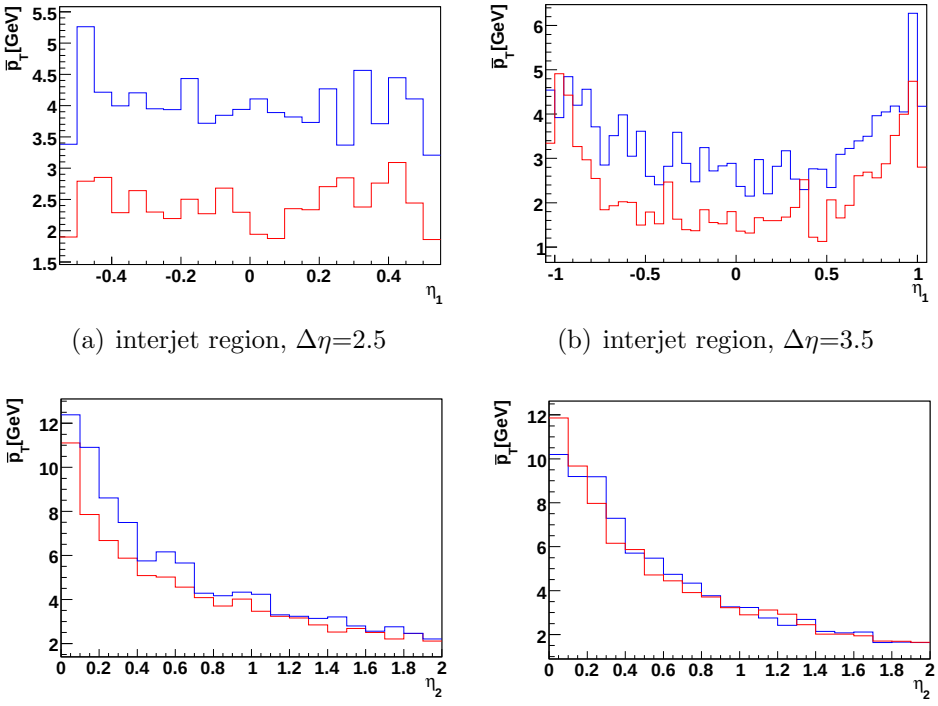

(a) interjet region, $\Delta\eta$=2.5

(b) interjet region, $\Delta\eta$=3.5

(c) away region, $\Delta\eta$=2.5

(d) away region, $\Delta\eta$=3.5

Figure 2.11: p_T distribution in the interjet region for events with UE. Red lines are for g^* events. Blue lines are for γ^* events.

2.3.5 Distribution of Jets with $p_T > 30$GeV in Events at $\Delta\eta < 2$

From the above analysis, the radiation difference between g^* and γ^* events is more apparent when $\Delta\eta$ is small, where η is pseudorapidity in the lab frame. Here, events with the top jets η_{jet_1} and η_{jet_2} in the range $-1 < \eta_{jet_1}, \eta_{jet_2} < 1$ are studied, where the interjet region is limited or even non-existent. The average distribution of number of jets with $p_T > 30$GeV is shown in figure 2.12. The difference is concentrated in the region $-2 < \eta < 2$. $p_T^{cut} = 30$GeV could clearly avoid the effect of the UE very well.

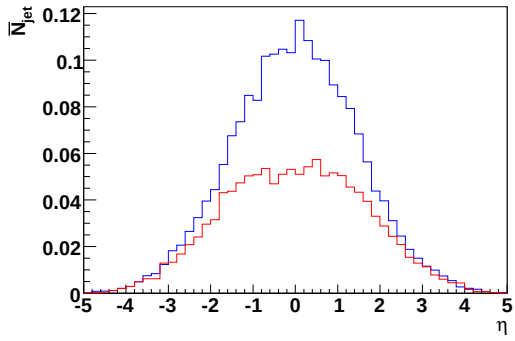

(a)

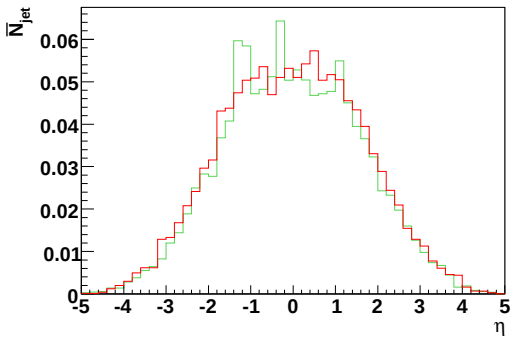

(b)

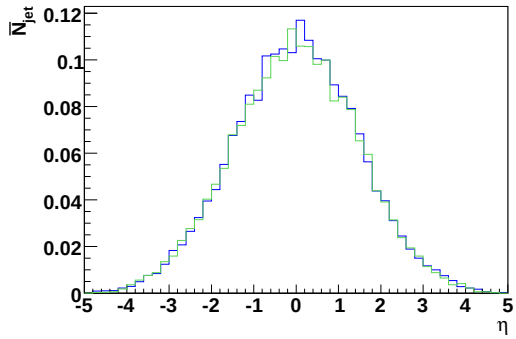

(c)

Figure 2.12: Distribution of jets with $p_T > 30$GeV in events with UE and with $-1 < \eta_{jet_1}, \eta_{jet_2} < 1$. η is pseudorapidity in the lab frame. (a)Comparison between the distribution of g^*(red line) and γ^*(blue line) events with UE.(b)Comparison between the distribution of g^* events with(red line) and without(green line) UE.(b)Comparison between the distribution of γ^* events with(blue line) and without(green line) UE.

2.4 Analysis Using Energy Flow

In this section, colour flow is studied through energy flow. Energy flow Q_c is the total transverse energy of all final-state particles in the interjet region. The energy distribution in the away region is also presented. Events with $\Delta\eta$ at $2.0, 2.5, 3.0, 3.5, 4.0$(with a spread of 0.1, e.g. 1.9 to 2.1) are studied.

2.4.1 Gap Fractions

Here the rapidity gap events are events in which energy flow Q_c is less than an energy threshold Q_0. Q_0 is selected to be: $10, 20$ and 30GeV. Consistent with the result from gap fractions defined by jet $p_T > p_T^{cut}$, $f_{gap}^{g^*}$ is always higher, as shown in figure 2.13. From the results of the last section, there are small p_T jets distributed over all phase space, the transverse energy of which are all included in Q_c. As a result, f_{gap} decreases rapidly when Δy increases. Gap fractions defined by jets with $p_T > p_T^{cut}$ have a better ability to avoid the effect of the UE.

The UE has a larger effect on gap fractions defined by energy flow. The difference between the f_{gap} curve for g^* events with UE and the f_{gap} curve for γ^* events without UE is still large enough to discriminate at $\Delta\eta = 2.5$. This difference becomes smaller when $\Delta\eta$ increases. The difference at $\Delta\eta = 3.5$ is much smaller than that of gap fractions defined by jets with $p_T > p_T^{cut}$ in figure 2.2.

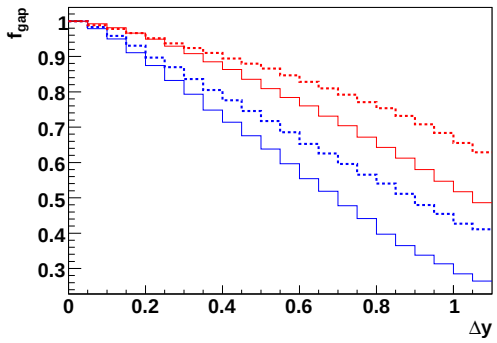

(a)

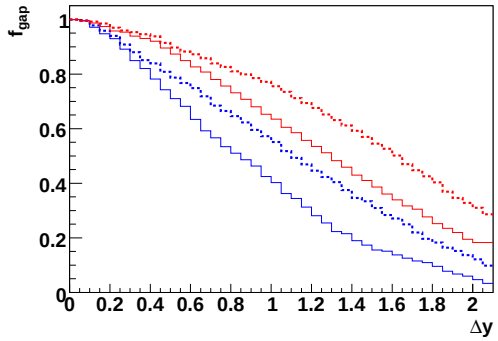

(b)

Figure 2.13: Gap fractions as functions of rapidity range defined by energy flow, (a)$\Delta\eta = 2.5$, $Q_0 = 30$GeV and (b)$\Delta\eta = 3.5$, $Q_0 = 30$GeV. Red solid lines are for g^* events with UE. Red dashed lines are for g^* events without UE. Blue solid lines are for γ^* events with UE. Blue dashed lines are for γ^* events without UE.

2.4.2 Gap Fraction as a Function of Energy Threshold

In this section, we study the gap fraction as a function of the energy threshold Q_0. According to Sung's study, the cross section of soft radiation could be expressed as a function of the parameter Q_0. In figure 2.14, a comparison is made between gap fractions in Sung's paper and results from events with and without UE at $\Delta\eta = 2$. The width of the interjet region in Sung's paper [23] is $Y = 1.5$, while $Y = \Delta\eta - 1.4$ is chosen here. Another difference is that the cross section in Sung's paper is at parton level rather than the full hadron level calculation we perform. There are some differences between the gap fractions from theory and this analysis. The concave shape of $f^{\gamma^*}_{gap}$ does not appear. $f^{g^*}_{gap}$

of events without UE is closer to the theoretical one, while it is smaller at low Q_0 and larger at large Q_0. $f_{gap}^{\gamma^*}$ of events with UE is closer to the theoretical one at low Q_0, while it is larger at large Q_0. f_{gap} in Sung's paper and from MC simulation tend to 1 when Q_0 is around 700GeV, which is the upper limit on the E_T of emissions. Figure 2.14(b) shows that the UE washes out the difference between $f_{gap}^{g^*}$ and $f_{gap}^{\gamma^*}$ badly at low Q_0.

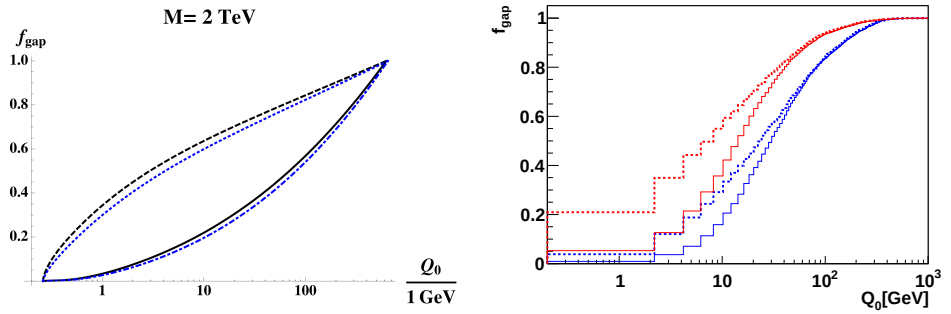

(a) (b)

Figure 2.14: Gap fractions as a function of Q_0 defined by energy flow at $\Delta\eta = 2$. (a)f_{gap} from Sung's paper. The solid black curve is for color-singlet events, and the dashed black curve is for color-octet events in which a heavy resonance decays into a top-quark pair. (b)f_{gap} of events with and without UE. The red solid line is for g^* events with UE. The red dashed line is for g^* events without UE. The blue solid line is for γ^* events with UE. The blue dashed line is for γ^* events without UE.

2.4.3 Energy Distribution

Energy distributions of final-state particles averaged over all events, which are the average energy distributions and denoted by $\bar{E}_T$, are studied in this section. The average energy flow of γ^* events is more than that of g^* events in the interjet region, which is shown in figure 2.15. As $\Delta\eta$ becomes larger, transverse energy per pseudorapidity $\Delta E_T/\Delta\eta_1$ will decrease in the central interjet region and increase in the region close to the top jets. In the interjet region, the value of the energy distributions of events without UE are less than those with UE, while the difference between g^* and γ^* is not spoiled.

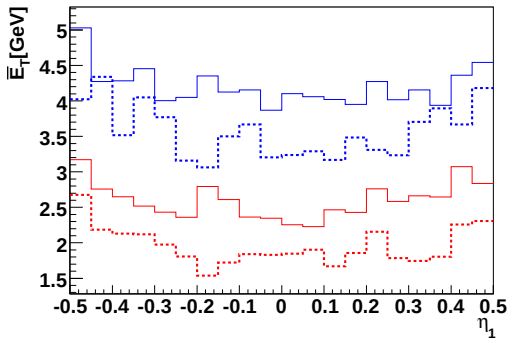

(a)

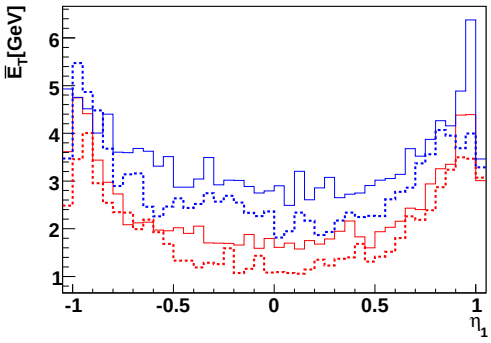

(b)

Figure 2.15: E_T distribution in the interjet region in events with and without UE at (a)$\Delta\eta = 2.5$, and (b)$\Delta\eta = 3.5$. The red solid lines are for g^* events with UE. The red dashed lines are for g^* events without UE. The blue solid lines are for γ^* events with UE. The blue dashed lines are for γ^* events without UE.

2.4.4 Q_c Distribution

The distribution of energy flow, Q_c, which is the total transverse energy of final-state particles in the interjet region, is studied in this section. Q_c is usually higher in γ^* events. This distribution gives a reference to choose Q_0. For example, when $\Delta\eta = 3.0$, it is sensible to choose $Q_0 = 40$GeV, considering the uncertainty of the UE, as shown in figure 2.16.

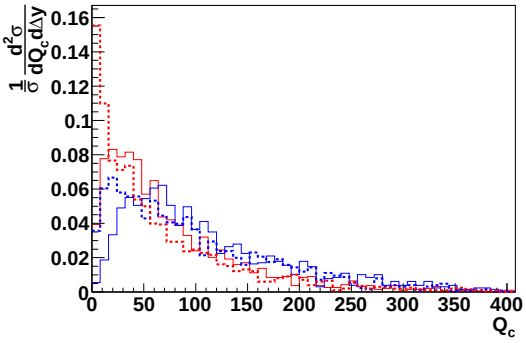

Figure 2.16: The Q_c distribution of g^* events and γ^* events at $\Delta\eta$=3.0 in events with and without UE. The red solid line is for g^* events with UE. The red dashed line is for g^* events without UE. The blue solid line is for γ^* events with UE. The blue dashed line is for γ^* events without UE.

2.5 $\Delta\eta$ Distribution

Comparison between the $\Delta\eta$ distribution shows that $\Delta\eta$ tends to be smaller in γ^* events, as shown in figure 2.17. Since the distributions of events with and without UE are similar, the difference comes from the effect of ISR and FSR of the outgoing jets of the hard process during the jet evolution. This is a manifestation of the "string effect" [38].

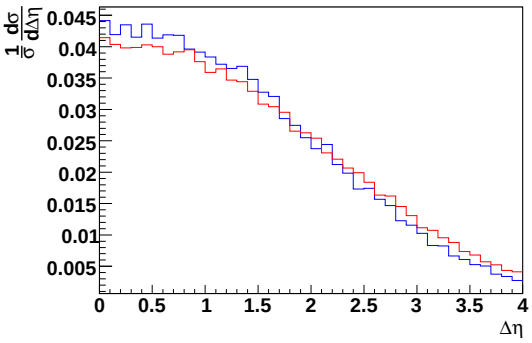

(a)

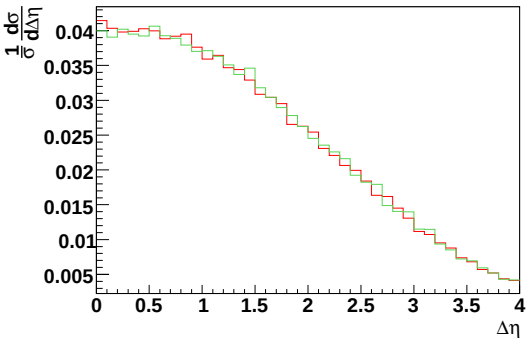

(b)

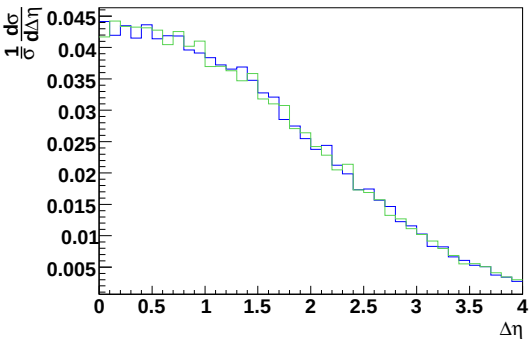

(c)

Figure 2.17: (a)$\Delta\eta$ distribution of g^* events(red line) and γ^* events(blue line). (b)Comparison between $\Delta\eta$ distribution of g^* events with(red line) and without(green line) UE. (c)Comparison between $\Delta\eta$ distribution of γ^* events with(blue line) and without(green line) UE.

Chapter 3

Analysis Using Spherical Harmonic Power Spectrum

In this chapter, the angular distribution of the transverse energy of final-state particles in g^* and γ^* events is studied using a spherical harmonic spectrum. In particular, the transverse energy correlations among final-state particles are considered. The spherical harmonic power spectrum contains the same information as a two-point correlation function. In order to study the E_T correlations among particles coming from different processes, we explore power spectra for (a)all final-state particles; (b)only those final-state particles within the top jets, where the QCD background from dijet events is also studied; (c)all final-state particles except those in the top jets.

3.1 Theory Background

A distribution on a sphere in $\theta - \phi$ space can be expanded into a spherical harmonic series. In this study, the transverse energy E_T is considered. The expansion is of the form,

$$E_T = \sum_{l} \sum_{m=-l}^{m=l} a_{lm} Y_{lm}(\theta, \phi) \tag{3.1}$$

where the spherical harmonic is related to the associated Legendre polynomial by

$$Y_{lm}(\theta,\phi) = \left[\frac{2l+1}{4\pi}\frac{(l-m)!}{(l+m)!}\right]^{1/2} P_l^m(\cos\theta)e^{im\phi} \tag{3.2}$$

In particular, Y_{l0} is independent of ϕ:

$$Y_{l0}(\theta) = \sqrt{\frac{2l+1}{4\pi}}P_l(\cos\theta) \tag{3.3}$$

The index l is related to the wavelength of spherical harmonics and m depends on the orientation of the polar coordinates. The coefficient a_{lm} is related to both the azimuth angle and the choice of polar coordinates.

The E_T correlation of two points (θ_1,ϕ_1) and (θ_2,ϕ_2) is defined as

$$C(\theta_{12}) = \langle E_T(\theta_1)E_T(\theta_2)\rangle \tag{3.4}$$

where θ_{12} is the angle between the directions given by θ_1 and θ_2, and the angle brackets mean the average over E_T of all pairs of directions seperated by θ_{12}.

Due to the orthogonality of spherical harmonics,

$$\left\langle \sum_l \sum_{m=-l}^{m=l} Y^*_{lm}(\theta_1,\phi_1) \sum_{l'} \sum_{m'=-l'}^{m'=l'} Y_{l'm'}(\theta_2,\phi_2) \right\rangle = \left\langle \sum_l \sum_{m=-l}^{m=l} Y^*_{lm}(\theta_1,\phi_1) Y_{lm}(\theta_2,\phi_2) \right\rangle \tag{3.5}$$

Hence, the average of the coefficients

$$\langle a_{lm}a_{l'm'}\rangle \propto \langle a_{lm}a_{l'm'}\rangle \delta_{ll'}\delta_{mm'} \tag{3.6}$$

Because of the unitarity attribute of spherical harmonics, the sum of spherical harmonics over m is unchanged in a different polar coordinate system,

$$\sum_{m=-l}^{m=l} Y^*_{lm}(\theta_1,\phi_1)Y_{lm}(\theta_2,\phi_2) = \sum_{m=-l}^{m=l} Y^*_{lm}(\theta_1^{'},\phi_1^{'})Y_{lm}(\theta_2^{'},\phi_2^{'}) \tag{3.7}$$

where the primed coordinate is in another polar coordinate system. The sum only depends on the θ difference between the points, not ϕ. If choosing the pole so that one point is at the pole, for example, $\theta_1 = 0$, the only nonvanishing

spherical harmonic is Y_{l0} and the sum becomes:

$$\sum_{m=-l}^{m=l} Y^*_{lm}(\theta_1,\phi_1)Y_{lm}(\theta_2,\phi_2) = Y^*_{l0}(0)Y_{l0}(\theta_{12}) = \frac{2l+1}{4\pi}P_l(\cos\theta_{12}) \tag{3.8}$$

Then the E_T correlation becomes,

$$C(\theta_{12}) = \sum_l \sum_{m=-l}^{m=l} \langle a_{lm}a_{l'm'}\rangle \frac{2l+1}{4\pi}P_l(\cos\theta_{12}) \tag{3.9}$$

C_l is defined to be the average power over modes m. It is called the power spectrum, or power spectrum density:

$$\langle a_{lm}a_{l'm'}\rangle = C_l\delta_{ll'}\delta_{mm'} \tag{3.10}$$

$$C_l = \frac{1}{2l+1}\sum_{m=-l}^{m=l} a^*_{lm}a_{lm} \tag{3.11}$$

This is analogous to the power spectrum in plane geometry, which is conventionally averaged over sinusoids with the same wave number. Since it is the sum of the squared modulus averaged over m, C_l is independent of both the azimuth angle and the polar coordinate system.

Using equations (3.5−3.11) above, the correlation function can be expressed as:

$$C(\theta_{12}) = \sum_l \frac{2l+1}{4\pi}C_lP_l(\cos\theta_{12}) \tag{3.12}$$

3.2 The Transformation

We use the package S2kit [39] to do discrete spherical harmonic transformations. Given a bandwidth B, the package does a transformation up to $l = B-1$,

$$f(\theta,\phi) = \sum_{l=0}^{l=B-1}\sum_{m=-l}^{m=l} a_{lm}Y_{lm}(\theta,\phi) \tag{3.13}$$

The coefficients a_{lm} of degree $l \geq B$ are equal to zero. 10000 g^* and γ^* events (with UE) are used for the spherical harmonic transformations, without discriminating between the position and the pseudorapidity difference of the

top jets. Final-state particles are clustered using fastjet, the anti-kt algorithm with a radius $R = 0.7$. The input values to S2kit are the transverse energies of final-state particles in jets with $p_T > 1\text{GeV}$. The values are sampled on $2B \times 2B$ equally spaced grids in $\theta - \phi$ space with a resolution of π/B. The top jets are identified as the two jets with largest p_T.

3.3 Some Features of the Power Spectrum

Spherical harmonic transformations decompose a distribution on a sphere into waves with different wavelengths. The wavelength corresponding to degree l is approximately π/l.

If the input information has changes on a small scale corresponding to a certain degree l', the value of degrees $l < l'$ (corresponding to larger size correlations) will not be affected much. The changes are mainly indicated by degrees $l \geq l'$.

Unlike the temperature anisotropy studied in CMB radiation, the input E_T values are discrete and have a large variance. In applications of the power spectrum in signal processing, delta functions in the time domain will leave a flat spectrum at high degrees, which is defined as white noise. In a spherical harmonic transformation, one discrete single bin acts like white noise and has the same effect on the power spectrum.

In the study of event structure, the E_T correlations on a large scale are considered. Transformations with bandwidth $B = 32$ can describe the shape of the input event sample quite well. Actually, we shall only consider multipoles with degree $l \leq 11$. Degree $l = 10$ corresponds to a scale of about 0.3 radian. This avoids the effects of fluctuations on a small scale and white noise.

If the E_T distribution is continuous and following a Gaussian distribution, the spectrum will decrease monotonically with increasing degree at low degrees. If E_T clusters on a certain scale, the magnitude of the corresponding multipole in the spectrum will have a higher value than the neighboring ones. An example event to illustrate this is shown in figure 3.1. Also shown is the inverse transformation. In the spectrum, even degrees have higher values than their neighboring multipoles. The inverse transformation is performed with only coefficients of the degree $l = 2$ or $l = 10$. Others are set to zero. In comparison with the true distribution of all final-state particles in figure 3.1(a), the

range of higher values(red and yellow) in the inverse transformation correctly corresponds to a cluster of E_T in the original sample.

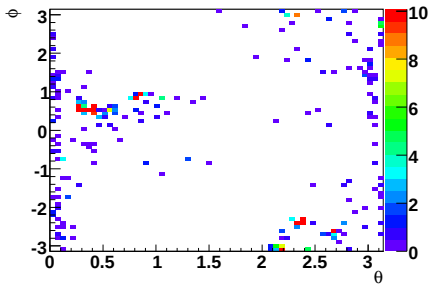

(a) A data sample of a g^* event. The top jets are removed, unit in GeV.

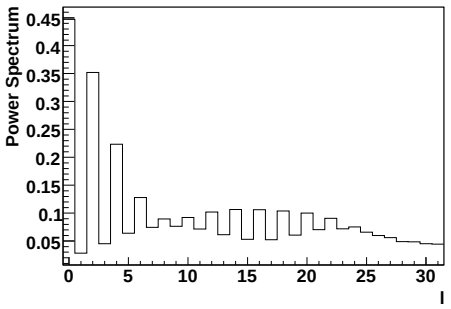

(b) The power spectrum

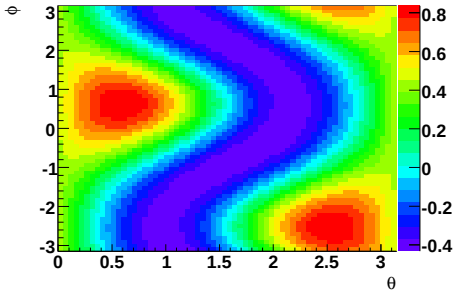

(c) Inverse transformation of coefficients of degree $l = 2$, unit in GeV.

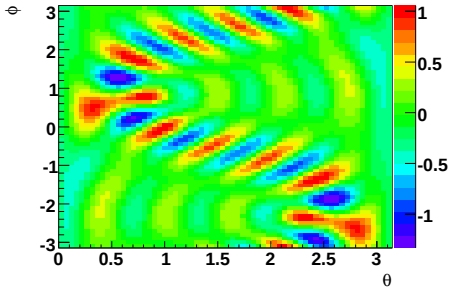

(d) Inverse transformation of coefficients of degree $l = 10$, unit in GeV.

Figure 3.1: Inverse transformation of coefficients of a certain degree for a g^* event.

The magnitude of degree $l = 1$ is usually small. Because the invariant mass of the two top jets is large, the two top jets are not much boosted and form an approximately back-to-back shape with even parity. The parity leads to even degrees with larger values than those of odd degrees next to them. The contribution of two back-to-back points, (θ, ϕ) and $(\pi - \theta, \pi + \phi)$, to the coefficients a_{lm} of odd degrees will be cancelled. As in the formula,

$$a_{lm} = \int_0^{2\pi} d\phi \int_0^{\pi} d\theta \sin\theta f(\theta, \phi) Y^*_{lm}(\theta, \phi) \tag{3.14}$$

$\sin\theta$ and $\sin(\pi - \theta)$ are opposite with other terms identical.

3.4 Average Power Spectrum and Standard Deviation

In this section, the input samples correspond to the transverse energies of all final-state particles in jets with $p_T > p_T^{min}$, or those particles only in the top jets or those in all jets excluding the top jets.

3.4.1 All Jets with $p_T > p_T^{min}$

The input sample of power spectrum of all jets are final-state particles in all jets with $p_T > 1$GeV. The average power spectrum is averaged over 10000 events with one power spectrum per event. The error bar is calculated by $Y/\sqrt{N}$, in which Y is the mean value of C_l, the value of degree l of the power spectrum, and $N = 10000$. The standard deviation is calculated by

$$s_l = \sqrt{\frac{1}{N-1}\sum_{i=1}^{N}(C_l^i - \bar{C}_l)^2} \tag{3.15}$$

where C_l^i is the value of degree l in the power spectrum of the ith event, and $\bar{C}_l$ is the average value of degree l over 10000 events. The error bar and standard deviation in following sections follow the same calculation.

The average power spectrum and standard deviation are shown in figure 3.2. The differences between γ^* and g^* are large. As mentioned above, multipoles with large magnitudes usually correspond to large values at the top-jet region in the inverse transformation. The higher values of even low degrees in the average power spectrum of g^* events indicate that the top jets and particles around them have larger proportion of the total E_T. The ratio of the E_T of the top jets to the total E_T of all jets is shown in figure 3.3.

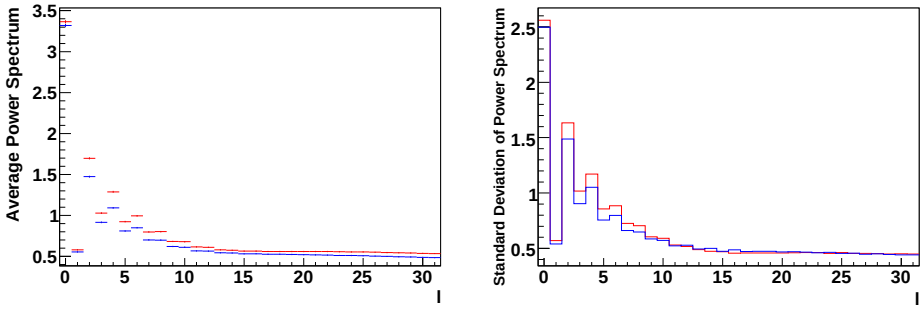

(a) (b)

Figure 3.2: Power spectrum of all final-state particles in jets with $p_T > 1$GeV. (a)Average power spectrum. (b)Standard deviation of power spectrum. Red lines are for g^* events and blue lines are for γ^* events.

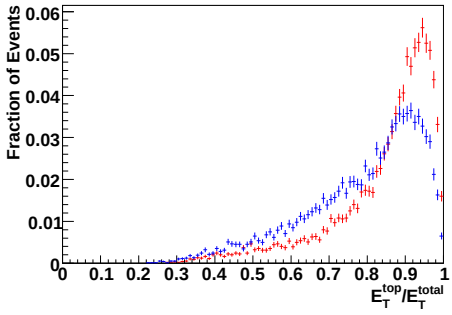

Figure 3.3: The proportion of the top jets E_T to the total E_T. The red line is for g^* events, and the blue line is for γ^* events.

3.4.2 The Top Jets

The average power spectrum of only the top jets are shown in this part. The average power spectrum of the top jets in g^* events is larger than that of γ^* events, as shown in figure 3.4. This is because the top jets in g^* events have larger E_T than those in γ^* events even when the masses of the resonances are same, due to less radiation. In the average normalized power spectrum, the even degrees are higher in the g^* case, which may come from the fact that the top jets in g^* events are more centralized, which is also comes from less radiation. The size of the top jets approximately corresponds to the degree at which the power spectrum turns to be flat, in relation $\theta = \pi/l$. The values of

the average power spectrum in figure 3.4 are almost identical to those in figure 3.2 except the values of degree $l = 0$. This is because the top jets dominate the shape of the power spectrum, as shown in figure 3.5. This motivates us to remove the top jets from the input sample.

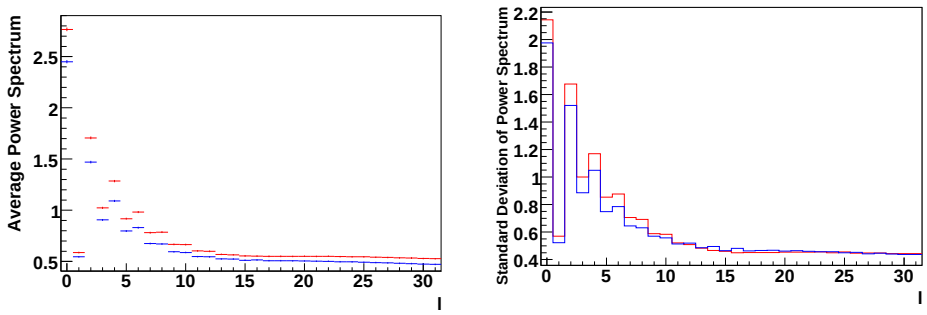

(a) (b)

Figure 3.4: Power spectrum of final-state particles in the top jets. (a)Average power spectrum. (b)Standard deviation of power spectrum. Red lines are for g^* events. Blue lines are for γ^* events.

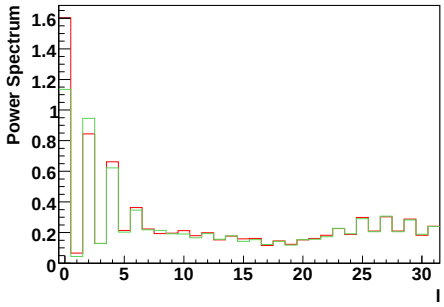

Figure 3.5: An example of power spectrum of all jets(red line) and only the top jets(green line) in a g^* event.

3.4.3 Jets Except the Top Jets

The power spectrum of final-state particles in all jets except the top jets contains information about energy correlations between particles other than particles in the top jets. Power spectra of final-state particles in jets with $p_T > 1, 5, 20\text{GeV}$ are shown in figure 3.6, with standard deviation shown in figure 3.7. The average normalized power spectrum, which is the average of the power spectrum normalized by the value of degree $l = 0$, is also shown.

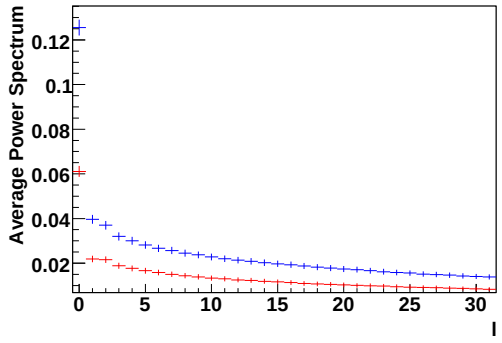

(a)

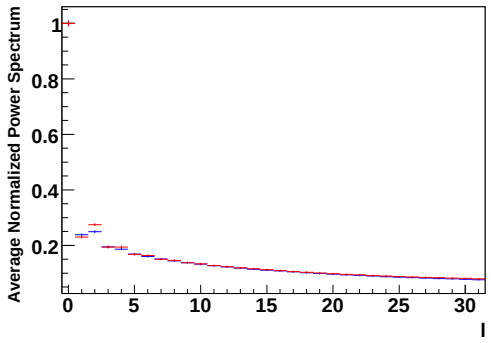

(b)

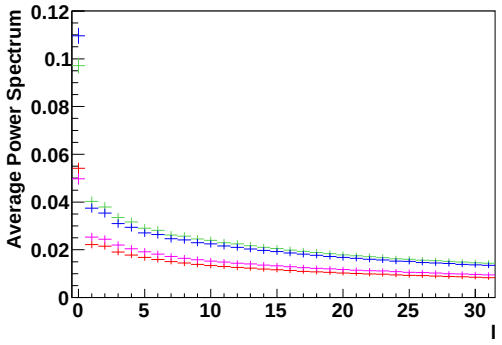

(c)

Figure 3.6: Power spectrum of final-state particles in jets except the top jets. (a)In jets with $p_T^{min} = 1$GeV. (b)Average normalized power spectrum of particles in jets with $p_T^{min} = 1$GeV. The value of degree $l = 0$ in the blue line is 1. Red lines are for g^* events and blue lines are for γ^* events. (c)In jets with $p_T^{min} = 5$GeV and $p_T^{min} = 20$GeV. The red line is for g^* events with $p_T^{min} = 5$GeV. The pink line is for g^* events with $p_T^{min} = 20$GeV. The blue line is for γ^* events with $p_T^{min} = 5$GeV. The green line is for γ^* events with $p_T^{min} = 20$GeV. Only events containing jets except the top jets with $p_T > p_T^{min}$ are included.

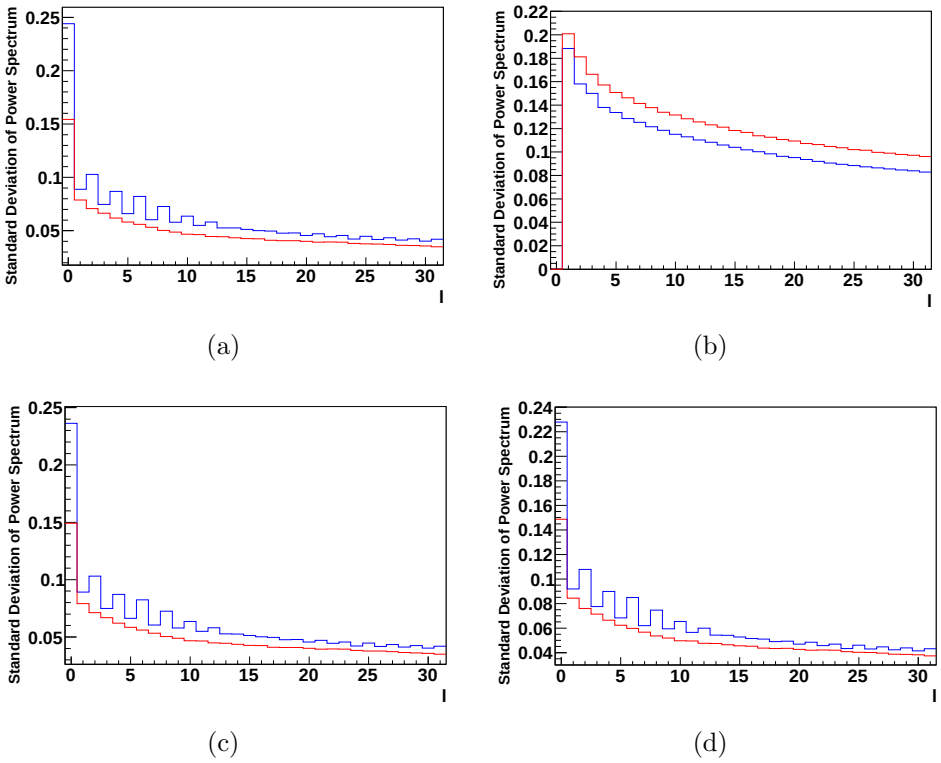

Figure 3.7: Standard deviation of power spectrum of final-state particles in jets except the top jets. (a)In jets with $p_T^{min} = 1$GeV. (b)Average normalized power spectrum of particles in jets with $p_T^{min} = 1$GeV. (c)In jets with $p_T^{min} = 5$GeV. (d)In jets with $p_T^{min} = 20$GeV. Red lines are for g^* events and blue lines are for γ^* events.

There is a very large difference between the average power spectra in this case, as shown in figure 3.6(a). The average normalized power spectrum shows that the two are very similar except the magnitudes of degree $l = 2$, which implies that the effect of different radiation has much the same effect over all scales. Compared with the average power spectrum with $p_T > 1$GeV, degree $l = 0$ in the average power spectrum with $p_T > 5$GeV is smaller and other degrees have very little difference. This indicates that the effect of jets with $p_T < 5$GeV on the power spectrum is mainly at degree $l = 0$(large scales). The difference at degrees other than $l = 0$ between power spectra with $p_T > 5$GeV and $p_T > 20$GeV shows that jets with $5\text{GeV} < p_T < 20\text{GeV}$ have effect on small scales.

The uncertainty due to the UE on the power spectrum should also be

considered. Comparison between average power spectrum of events with and without UE is shown in figure 3.8. A significant difference occurs at degree $l = 0$, which may indicate the additional products from the UE spread widely. Differences at degrees $l \geq 1$ are small within uncertainties. The effect of the UE is tiny. We can easily distinguish g^* from γ^* using power spectrum method.

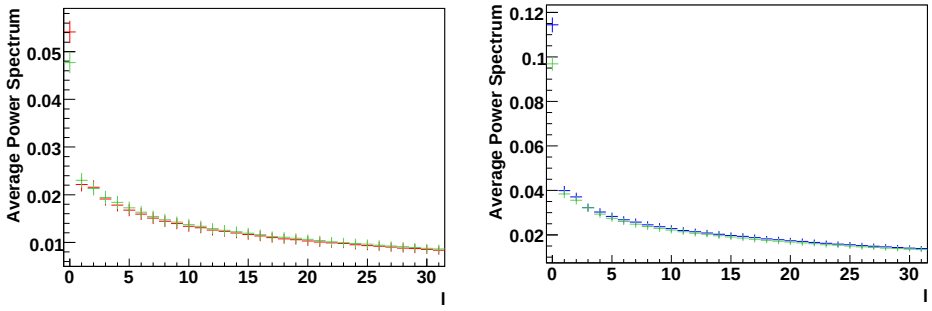

(a) $p_T^{cut} = 5\text{GeV}$, g^* (b) $p_T^{cut} = 5\text{GeV}$, γ^*

Figure 3.8: The average power spectrum of final-state particles in jets except the top jets with $p_T^{cut} = 5\text{GeV}$. Comparisons between the power spectra of events with and without UE. Red lines are for g^* events with UE. Blue lines are for γ^* events with UE. Green lines are for events without UE.

3.4.4 The Difference Between Hadronically decaying top jets and QCD jets

In this part we apply the power spectrum to the final-state particles in a single jet. The samples used are QCD events with all possible processes and g^* and γ^* events with both tops decaying hadronically. The two leading jets defined by anti-kt algorithm with $R = 0.7$ are selected. Only the jet with larger p_T is used. To make the QCD jets similar to the top jets, the following cuts are applied: the invariant mass of the two leading jets, $M_{jets}^{inv} > 1500\text{GeV}$; the invariant mass of each leading jet, $150\text{GeV} < M_{jet}^{inv} < 200\text{GeV}$. The particles in the leading jet are clustered using anti-kt algorithm with $R = 0.3$. The difference between the E_T of the leading jet and its leading subjet is examined. As shown in figure 3.9, the distribution of $\Delta E_T/E_T$, which is the proportion of the difference between the E_T of the jet and the leading subjet, denoted by ΔE_T, to the E_T of the jet, is different between the QCD jets and top jets. Most QCD jets accumulated at the region $\Delta E_T/E_T < 0.1$, which indicates

that the E_T of the QCD jets are concentrated in a smaller range. The average power spectra of the QCD events and KK-particle events with $\Delta E_T/E_T < 0.1$ are shown in figure 3.10. Since the QCD jets have larger E_T, the values of average power spectrum are higher. The average normalized power spectrum of QCD jets shows that the higher degrees have larger value, which indicated that the size of the subjet of the QCD jets which contain most E_T is smaller. This is a first study and it would be useful to do this with QCD events which, for example, pass the Johns Hopkins top tagger [40].

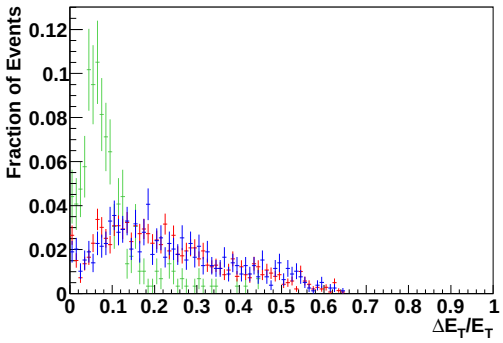

Figure 3.9: The difference between E_T of the leading jet and its subjet. The green line is for QCD events. The red line is for g^* events. The blue line is for γ^* events.

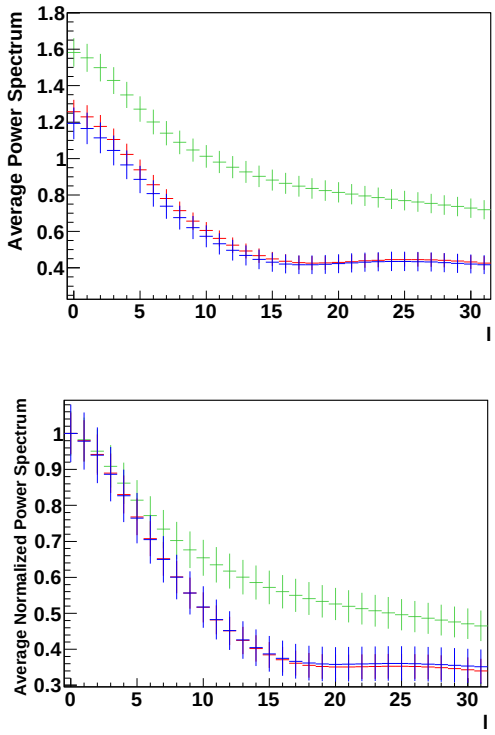

Figure 3.10: The average power spectra of QCD events and KK-particle events with $\Delta E_T/E_T < 0.1$. (a)Average power spectrum. (b)Average normalized power spectrum. The green lines are for QCD events. The red lines are for g^* events. The blue lines are for γ^* events.

Chapter 4

Conclusion

Recently, Sung studied the different patterns of soft gluon radiation in new TeV-scale resonance events due to the different colour contents. This study provides a promising way to distinguish colour-singlet and colour-octet particles in new physics. From theoretical calculations, there is a large difference between the gap fractions for the two kinds of events.

This study is focussed on the colour difference of the new resonances. The particles studied are g^* and γ^*. The analysis is undertaken using both rapidity gap events and the spherical harmonic spectrum. Events in which two top jets have large pseudorapidity difference are studied through additional jets and energy flow. The gap fraction is evaluated using two methods. A gap fraction defined by jets with p_T above a given value could avoid the effect of the UE better than that defined by energy flow. The number of jets with p_T above a given value is compared between g^* and γ^* events. It is found that when the pseudorapidity difference of the top jets is large, the uncertainty of the UE can spoil the discriminating ability when there is one additional jet with $p_T > p_T^{cut}$ in the interjet region. For events which do not contain a rapidity gap, the distribution of jets with $p_T > p_T^{cut}$ is studied. It is found that the average number of jets with $p_T > p_T^{cut}$ in the central interjet region is higher for γ^* events. This phenomenon is more apparent when the pseudorapidity difference between the two top jets is small. The jet number and energy distribution are also studied in the top-jet region and the region between the top jets and the beams. There are small differences in the latter case. In the top-jet region, the proportion of events containing jets with $p_T > 30$GeV is about 0.2 higher in γ^* events than in g^* events when $\Delta\eta$ is small.

In the study of the spherical harmonic spectrum, the average power spectra of the full event, of final-state particles in the top jets and of those particles in jets excluding the top jets are compared between g^* and γ^* events. The difference of the average power spectrum of final-state particles in jets except the top jets is very large. The effect of the UE on the average "except-top-jet" power spectrum is mainly at degree $l = 1$.

It remains to be seen how the power spectrum methods discussed here can be used in other circumstances. Certainly the results in Chapter 3 are encouraging.

Bibliography

[1] Steven Weinberg. *The Quantum Theory of Fields, Vol.3:Supersymmetry*. Cambridge University Press, Cambridge, England, 2005.

[2] Nima Arkani-Hamed, Savas Dimopoulos, and G. R. Dvali. The hierarchy problem and new dimensions at a millimeter. *Phys. Lett.*, B429:263–272, 1998.

[3] Lisa Randall and Raman Sundrum. Large mass hierarchy from a small extra dimension. *Phys. Rev. Lett.*, 83(17):3370–3373, Oct 1999.

[4] Andrew R. Liddle and David H. Lyth. *Cosmological Inflation and Large-Scale Structure*. Cambridge University Press, 2000.

[5] Torbjorn Sjostrand, Stephen Mrenna, and Peter Z. Skands. A Brief Introduction to PYTHIA 8.1. *Comput. Phys. Commun.*, 178:852–867, 2008.

[6] Ben Lillie, Lisa Randall, and Lian-Tao Wang. The Bulk RS KK-gluon at the LHC. *JHEP*, 09:074, 2007.

[7] Ben Lillie, Jing Shu, and Timothy M. P. Tait. Kaluza-Klein Gluons as a Diagnostic of Warped Models. *Phys. Rev.*, D76:115016, 2007.

[8] Abdelhak Djouadi, Gregory Moreau, and Ritesh K. Singh. Kaluza–Klein excitations of gauge bosons at the LHC. *Nucl. Phys.*, B797:1–26, 2008.

[9] P. Osland, A. A. Pankov, A. V. Tsytrinov, and N. Paver. Signals of Warped Extra Dimensions at the LHC. *AIP Conf. Proc.*, 1317:201–208, 2011.

[10] Kaustubh Agashe, Adam Falkowski, Ian Low, and Geraldine Servant. KK Parity in Warped Extra Dimension. *JHEP*, 04:027, 2008.

[11] Brian Cox, Jeffrey R. Forshaw, and Leif Lonnblad. Hard color singlet exchange at the Tevatron. *JHEP*, 10:023, 1999.

[12] Jeffrey Forshaw, James Keates, and Simone Marzani. Jet vetoing at the LHC. *JHEP*, 07:023, 2009.

[13] Gianluca Oderda and George F. Sterman. Energy and color flow in dijet rapidity gaps. *Phys. Rev. Lett.*, 81:3591–3594, 1998.

[14] Carola F. Berger, Tibor Kúcs, and George Sterman. Event shape–energy flow correlations. *Phys. Rev. D*, 68(1):014012, Jul 2003.

[15] Sascha Bornhauser, Manuel Drees, Herbert K. Dreiner, and Jong Soo Kim. Rapidity Gap Events in Squark Pair Production at the LHC. *Phys. Rev.*, D80:095007, 2009.

[16] F. Chevallier, O. Kepka, C. Marquet, and C. Royon. Gaps between jets at hadron colliders in the next-to-leading bfkl framework. *Phys. Rev. D*, 79(9):094019, May 2009.

[17] Yu.L. Dokshitzer, V.A. Khoze, and S. Troyan. *in Physics in Collision VI, Proceedings of the International Conference*, volume 04. World Scientific, Singapore, Chicago, Illinois, 1986 edition, 1987.

[18] J. D. Bjorken. Rapidity gaps and jets as a new-physics signature in very-high-energy hadron-hadron collisions. *Phys. Rev. D*, 47(1):101–113, Jan 1993.

[19] Yu.L. Dokshitzer, V.A. Khoze, and T. Sjostrand. Rapidity gaps in higgs production. *Physics Letters B*, 274(1):116 – 21, 1992/01/02.

[20] Rikard Enberg, Gunnar Ingelman, and Nicusor Timneanu. Rapidity gaps at HERA and the Tevatron from soft color exchanges. *J. Phys.*, G26:712, 2000.

[21] M. Derrick et al. Observation of events with a large rapidity gap in deep inelastic scattering at HERA. *Phys. Lett.*, B315:481–493, 1993.

[22] S. Abachi et al. Jet Production via Strongly-Interacting Color-Singlet Exchange in $p\bar{p}$ Collisions. *Phys. Rev. Lett.*, 76:734–739, 1996.

[23] Ilmo Sung. Probing the gauge content of heavy resonances with soft radiation. *Phys. Rev. D*, 80(9):094020, Nov 2009.

[24] Torbjorn Sjostrand, Richard Corke, and Peter Skands. PYTHIA 8 worksheet. 18 January 2011, http://home.thep.lu.se/ torbjorn/pythia8/worksheet8140.pdf.

[25] S. Maus. The geomagnetic power spectrum. *Geophysical Journal International*, 174(1):135 – 42, 2008/07/.

[26] M. Korte, C.G. Constable, and R.L. Parker. Revised magnetic power spectrum of the oceanic crust. *Journal of Geophysical Research*, 107(B9):6 – 1, 10 Sept. 2002.

[27] Sujata Gupta and Alan F. Heavens. Peaks in the cmb—sensitively testing the gaussian hypothesis. *AIP Conference Proceedings*, 555(1):337–340, 2001.

[28] J. H. P. Wu et al. Tests for Gaussianity of the MAXIMA-1 CMB Map. *Phys. Rev. Lett.*, 87:251303, 2001.

[29] David Langlois. Isocurvature cosmological perturbations and the cmb. *Comptes Rendus Physique*, 4(8):953 – 959, 2003. Dossier: The Cosmic Microwave Background.

[30] Roni Harnik and Tommer Wizansky. Signals of new physics in the underlying event. *Phys. Rev. D*, 80(7):075015, Oct 2009.

[31] M. Campanelli and J. W. Monk. Fourier Transforms as a tool for Analysis of Hadron-Hadron collisions, 2009. hep-ph/0910.5108.

[32] Mrinal Dasgupta and Gavin P. Salam. Event shapes in e+ e- annihilation and deep inelastic scattering. *J. Phys.*, G30:R143, 2004.

[33] Leandro G. Almeida, Seung J. Lee, Gilad Perez, George Sterman, and Ilmo Sung. Template Overlap Method for Massive Jets. *Phys. Rev.*, D82:054034, 2010.

[34] Diego M. Hofman and Juan Maldacena. Conformal collider physics: Energy and charge correlations. *JHEP*, 05:012, 2008.

[35] Matteo Cacciari and Gavin P. Salam. Dispelling the N^3 myth for the k_t jet-finder. *Phys. Lett.*, B641:57–61, 2006. M. Cacciari, G.P. Salam and G. Soyez, http://fastjet.fr/.

[36] Matteo Cacciari, Gavin P. Salam, and Gregory Soyez. The anti-k_t jet clustering algorithm. *JHEP*, 04:063, 2008.

[37] F. V. Tkachov. Measuring the number of hadronic jets. *Phys. Rev. Lett.*, 73:2405–2408, 1994.

[38] Ya. I. Azimov, Yu. L. Dokshitzer, V. A. Khoze, and S. I. Troyan. The string effect and qcd coherence. *Physics Letters B*, 165(1-3):147 – 150, 1985.

[39] Peter J. Kostelec and Daniel N. Rockmore. S2kit: A lite version of spharmonickit, 2004.

[40] David E. Kaplan, Keith Rehermann, Matthew D. Schwartz, and Brock Tweedie. Top tagging: A method for identifying boosted hadronically decaying top quarks. *Phys. Rev. Lett.*, 101(14):142001, Oct 2008.